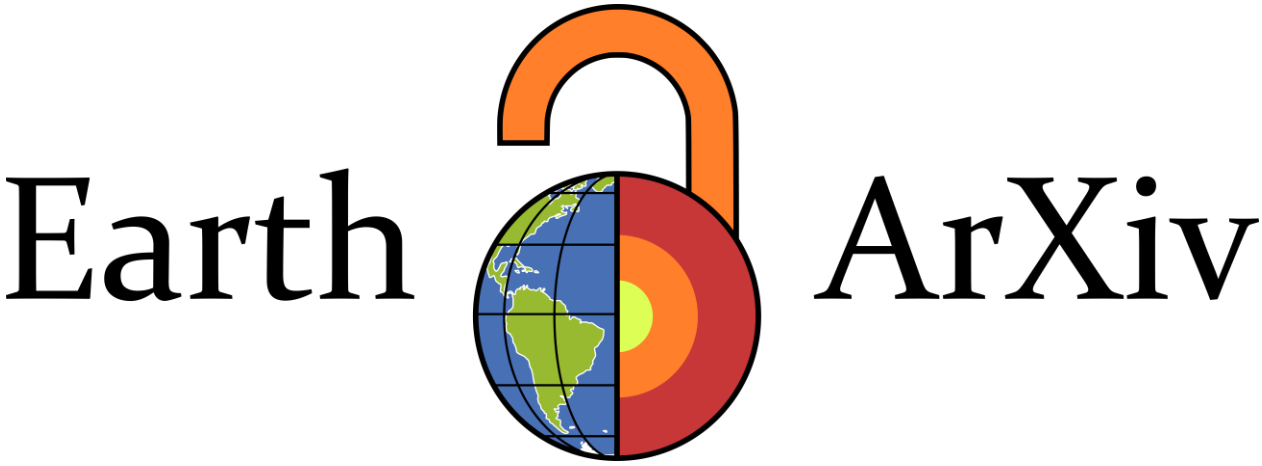

Assessing inversion uncertainty from initial-model variability in 3-D magnetotelluric inversion: Application to a geothermal field

Abstract

Magnetotelluric (MT) inversion is widely used to image subsurface electrical resistivity structures, but three-dimensional (3-D) MT inversion is inherently non-unique, and the resulting models can depend strongly on the choice of the initial model. Despite this well-known sensitivity, systematic evaluation of initial-model-induced variability remains uncommon in practical 3-D MT studies due to the high computational cost of running multiple inversions. In this study, we propose a practical and computationally efficient framework to quantify inversion uncertainty arising specifically from differences in the initial model. The approach employs a low-dimensional parameterization based on representative points and uses Kriging interpolation to generate an ensemble of smooth, geologically plausible starting models. Each realization is inverted independently using identical inversion settings, allowing initial-model effects to be isolated under fixed regularization and data-error assumptions. The method is applied to a 3-D MT dataset from the Yuzawa geothermal field in northeastern Japan. A total of 100 inversions were performed, from which 55 well-converged realizations (final RMS $\leq$ 2.15) were selected for analysis. Ensemble statistics reveal that shallow conductive structures are reproduced consistently across realizations, whereas variability increases with depth and exhibits strong spatial dependence. Bootstrap resampling confirms that the depth-dependent variability patterns are statistically stable under the present ensemble size. Although the proposed framework does not account for all possible sources of inversion uncertainty, it provides an operationally realistic lower-bound estimate of model variability associated with initial-model choice. By identifying which parts of the resistivity structure are robust and which are weakly constrained, the method supports uncertainty-aware interpretation of 3-D MT inversion results and demonstrates its practical applicability through a geothermal case study.

Keywords: Magnetotellurics, 3D inversion, initial model, uncertainty quantification, geothermal exploration, Kriging

Introduction

Magnetotellurics (MT) is a geophysical method widely used to image subsurface electrical resistivity structures and has been applied in a broad range of Earth science and resource exploration studies. With advances in computational power and numerical inversion algorithms, three-dimensional (3D) MT inversion has become increasingly common, enabling more detailed and quantitative characterization of complex subsurface structures (e.g., Kelbert et al., 2014; Li et al., 2025; Sasaki, 2004; Siripunvaraporn et al., 2005; Usui, 2015).

In principle, quantitative resistivity distributions can be estimated from surface-acquired MT data by minimizing an objective function that combines data misfit with regularization constraints. However, 3D MT inversion poses several fundamental challenges. The forward problem, which numerically simulates electromagnetic field propagation, must be solved repeatedly and is computationally expensive. More importantly, MT inversion is inherently ill-posed: the number of model parameters (cells) typically far exceeds the number of observations. As a result, the inversion yields only one realization from a non-unique, infinite family of models that can fit the data equally well (Muñoz & Rath, 2006; Causse, 2023).

This non-uniqueness arises from multiple factors, including data noise, regularization choices, model parameterization, and prior assumptions. Among these factors, previous studies have shown that the choice of the initial or prior model can exert a particularly strong influence on the final inversion result. Differences in the initial model have been reported to produce substantial variability in recovered resistivity structures, even when the same dataset, error floors, and regularization schemes are used (e.g., Robertson et al., 2020). Despite its recognized importance, systematic evaluation of initial-model dependence remains uncommon in practical 3D

MT studies, primarily because exploring multiple inversion realizations is computationally demanding.

Quantifying inversion uncertainty is therefore essential for reliable interpretation of MT-derived resistivity models. However, comprehensive uncertainty analysis remains challenging for large-scale 3D MT problems, particularly when realistic model sizes and survey geometries are considered. Fully Bayesian approaches provide a theoretically rigorous framework for uncertainty quantification, but their application to practical 3D MT inversions is often computationally prohibitive due to the high dimensionality of the model space and the cost of forward simulations (Manassero et al., 2020). These limitations motivate the development of uncertainty-evaluation strategies that are computationally feasible and compatible with existing inversion workflows.

In this study, we focus specifically on uncertainty arising from differences in the initial model. This focus is motivated by previous sensitivity studies, particularly Robertson et al. (2020), which demonstrated that initial-model choice is one of the dominant contributors to variability in 3D MT inversion results. We propose a simple and computationally efficient framework to evaluate initial-model-induced variability by generating an ensemble of smooth, geologically plausible starting models using a low-dimensional parameterization combined with Kriging interpolation.

To demonstrate the practical applicability of the proposed approach, we apply it to an existing 3D MT dataset acquired in a geothermal field (Ishizu et al., 2022). Although the method itself is general and applicable to a wide range of MT inversion problems, geothermal data provides a useful case study because MT-derived resistivity structures in such settings are commonly interpreted in terms of conductive features whose robustness is often of practical interest. By treating the geothermal dataset as an

application example, we illustrate how initial-model uncertainty can be quantified and how the resulting information can support more robust interpretation of MT inversion results in applied geophysical studies.

Methodology

1. Motivation for the Proposed Ensemble-Based Approach

We define the initial model dependence problem as:

$$\boldsymbol{m}(\boldsymbol{m_0}) = \arg\min_{m^*} F(\boldsymbol{m}^*, \boldsymbol{m_0}) \tag{1}$$

where $\boldsymbol{m_0} \in \mathbb{R}^N$ is an initial guess of the model parameters, N is the number of the model parameters, F is the objective function, and $\boldsymbol{m}(\boldsymbol{m_0})$ denotes the inversion result obtained from a given initial guess. The uncertainty due to different initial guesses can be evaluated from the ensemble of models $\boldsymbol{m}(\boldsymbol{m_0})$.

To efficiently obtain such an ensemble from the relevant parameter space, prior information—such as known geological structures or results from other geophysical methods—can be incorporated to define plausible resistivity ranges and generate initial models accordingly(Causse, 2023). However, MT is often used in preliminary surveys (e.g., Ogawa et al., 1997) during resource exploration or to image structures deeper than the reach of drilling (e.g., Ichiki et al., 2021; Zhang et al., 2025). In such cases, feasible resistivity ranges are often unknown.

A common approach in MT to examine sensitivity to the initial model is to test a few homogeneous starting models with different resistivity values (Robertson et al., 2020, Ishizu et al., 2022). However, this strategy explores only a very limited portion of the model parameter space. To obtain a broader understanding of inversion behaviour, we must explore a wider range of initial models.

One of the simplest approaches under this condition is to assign random resistivity values to each model cell. However, this method tends to introduce abrupt resistivity changes between neighboring cells, which can lead to numerical instability in the inversion. Moreover, the degrees of freedom in defining the initial model become excessively large, making the exploration of the parameter space inefficient.

Bayesian approaches, such as the reduced-order MCMC framework of Manassero et al. (2020), provide a rigorous characterization of inversion uncertainty. Their implementation, however, requires substantial algorithmic development—including the construction of reduced-order forward models and the design of specialized sampling schemes—and the MCMC sampling itself is not trivially parallelizable because successive samples are statistically dependent. As a result, these methods remain technically demanding to deploy in typical 3-D MT inversion workflows.

2. Initial Model Generation with Kriging Interpolation

To address these issues, we propose a hybrid approach based on the use of representative points and spatial interpolation and extrapolation. The algorithm consists of the following steps:

(1) Select representative points covering both the survey area and depth of interest,

(2) Assign random resistivity values within a reasonable range to these points,

(3) Use Kriging (Isaaks & Srivastava, 1989) to interpolate and extrapolate the values to all model cells used in the forward modeling,

(4) Run the inversion using the generated initial model,

(5) Repeat steps (2) through (4),

(6) Evaluate the resulting ensemble of models $\boldsymbol{m}(\boldsymbol{m_0})$ to quantify uncertainty.

This method reduces the dimensionality of the initial model space and enables more efficient exploration. Although simple, it provides flexibility in the selection and distribution of representative points. The proposed approach is conceptually similar to the use of "pilot points" in PEST, a model-independent parameter estimation and uncertainty analysis framework (Doherty et al., 2011). The method is also highly parallelizable, as each inversion is independent of the others. Therefore, near-linear speed-up can be expected with increasing numbers of computing nodes. This embarrassingly parallel structure makes the workflow practical for larger 3-D MT surveys. The flowchart of this method is shown in Figure 1.

Unlike conventional homogeneous starting models, which impose spatial uniformity and severely under-sample the plausible model space, the Kriging-based representative-point approach generates spatially structured, geologically plausible initial models while retaining computational feasibility. We adopt kriging because it provides smooth, spatially correlated resistivity fields consistent with geological expectations, while allowing us to control correlation length scales via the variogram.

While our method does not provide a formal posterior distribution, it highlights the range of plausible resistivity structures that may arise solely from changes in the initial model under fixed choices of the data-error model, regularization, and structural parameterization.

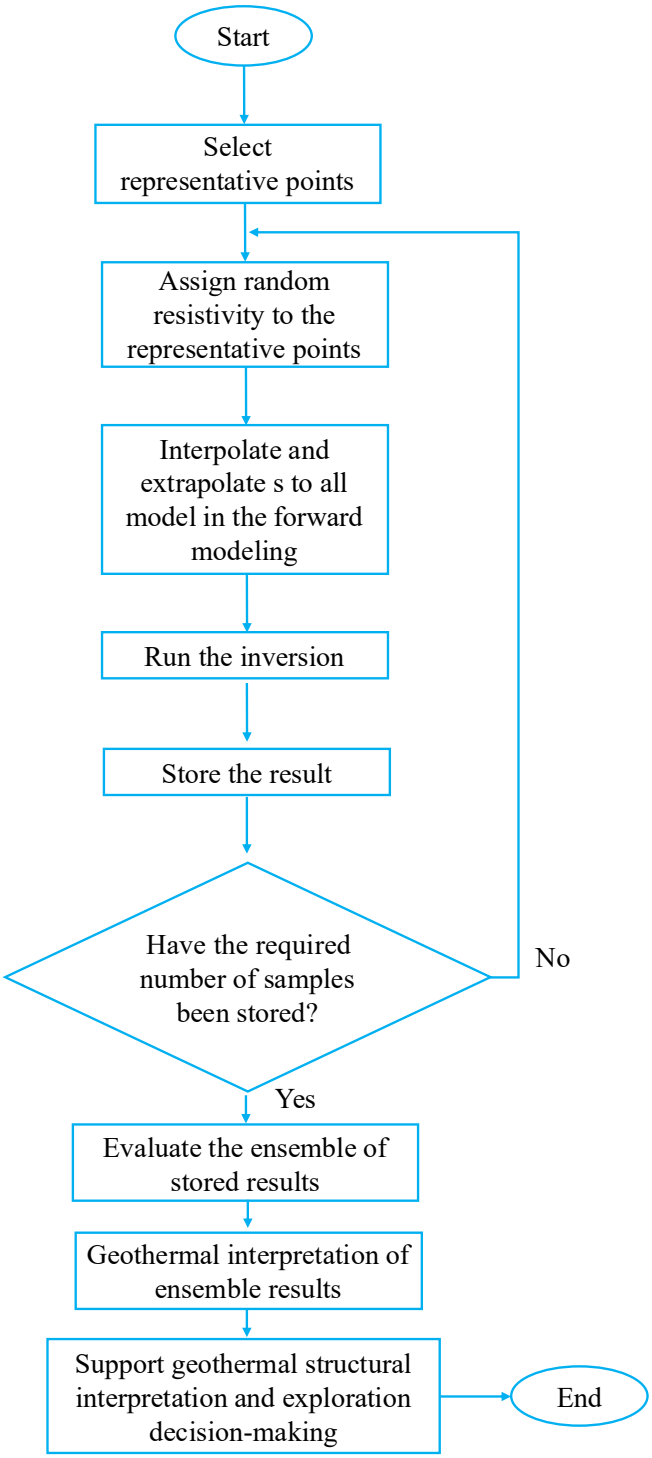

Figure 1

Flowchart illustrating the proposed approach for evaluating uncertainty arising from variations in initial models

3. MT Inversion

MT inversion in our case uses the impedance tensor Z and the tipper **T** as below:

$$\begin{pmatrix} E_x \\ E_y \end{pmatrix} = \begin{pmatrix} Z_{xx} & Z_{xy} \\ Z_{yx} & Z_{yy} \end{pmatrix} \begin{pmatrix} H_x \\ H_y \end{pmatrix}, \tag{2}$$

$$H_z = \begin{pmatrix} T_x & T_y \end{pmatrix} \begin{pmatrix} H_x \\ H_y \end{pmatrix} \tag{3}$$

where **E** is the electric fields, **H** is the magnetic field, $x, y,$ and z are the directions of the north–south, east–west, and vertical directions, respectively.

We define the objective function to match the calculated impedance tensor and the tipper with the observed ones, as below:

$$F(\mathbf{m}) = |\mathrm{W}\mathbf{d}_{\mathbf{obs}} - \mathrm{W}\mathbf{d}_{\mathbf{calc}}|^2 + \alpha^2 |\mathrm{R}\log(\mathbf{m})|^2 + \beta^2 \sum_{n=1}^{N_{obs}} \sum_{i=1}^{2} \sum_{j=1}^{2} \left(D_{ij}^n - I_{ij}\right)^2 \tag{4}$$

where $\mathbf{m}$ is the model parameters, $\mathbf{d}_{\mathbf{obs}}$ and $\mathbf{d}_{\mathbf{calc}}$ are the observed and calculated data (i.e., components of the impedance tensor and tipper), W is the weight matrix, R is the smoothness matrix, D^n is the distortion tensor, I is the identity matrix, N_{obs} is the number of the observation sites, α^2 and β^2 is the trade-off parameters for the model smoothness constraint and estimation of the distortion tensor. Note that MT inversion is usually the ill-posed problem, hence the solution depends on the initial model parameters. The detailed explanation of the inversion scheme is written in Suzuki (2025). The full workflow including the generation of initial model and MT inversion is shown in Algorithm 1.

Algorithm 1 Workflow for initial-model uncertainty analysis

1. Select representative points covering the model domain.
2. Draw random resistivity values at these points within a predefined log-scale range.
3. Use ordinary Kriging to interpolate/extrapolate these values to all model cells, producing a smooth initial model.
4. Perform a 3-D MT inversion using the trade-off sequence $\lambda = 10 \rightarrow 1 \rightarrow 0.1$.
5. Compute the final RMS misfit and retain the realization if RMS $\leq$ threshold.
6. Repeat steps 2–5 to generate the full set of realizations.
7. Compute ensemble statistics (mean model, standard deviation, depth-dependent spread).
8. Apply bootstrap resampling to assess the robustness of the spread estimates.
9. Interpret the spatial distribution of uncertainty in terms of geothermal structures (cap rock, deep conductive zones) to support risk-aware drilling and survey planning.

Data and Settings

We used MT data from thirty sites reported by Ishizu et al. (2022), in an area where several geothermal power plants are located (Figure 2).

As mentioned in the Introduction, we adopted the inversion code developed by Suzuki (2025). The model consisted of 34 × 34 × 62 cells (including 10 layers of air) along the north-south (X), east-west (Y), and vertical (Z) directions. A locally refined mesh was employed in the central part of the model to increase resolution in the area of interest. The total model extent was 200 km × 200 km × 160 km in the respective directions, with a total of 210,297 cells. The minimum cell sizes in the north-south,

east-west, and vertical directions are 400 m, 400 m, and 30 m, respectively. We used constant resistivity in the air (10^6 Ω·m) and sea (0.25 Ω·m) layers. We considered the topography using ETOPO 2022 (Macferrin et al., 2025; NOAA National Centers for Environmental Information, 2022) with the unstructured hexahedral cells.

Four components of the impedance tensor and two components of the tipper were used in the inversion. We set the error floors of the impedance tensor and the tipper to 5% of $\left|Z_{xy}Z_{yx}\right|^{\frac{1}{2}}$ and 15% of absolute values of the components, respectively. These settings were the same as Ishizu et al. (2022). A map of the survey area and model setup is shown in Figure 2 and Figure 3. Twelve frequency points were used, ranging from 100 Hz to 0.001 Hz. The trade-off parameters α^2 and β^2, as defined in Suzuki (2025), were set to the same value and successively reduced in the order of 10, 1, 0.1. We evaluated the final models when α^2 and β^2 equal to 0.1. A single reducing schedule was adopted for all realizations to maintain methodological consistency. Case-by-case tuning of the trade-off parameters was not attempted, as it would confound initial-model sensitivity with regularization sensitivity.

To generate the initial models, resistivity values at the representative points were randomly sampled on a $\log_{10}$ scale between 1 Ω·m and 1000 Ω·m. A total of 3 × 3 × 4 representative points were selected along the X, Y, and Z directions. The coordinates of the representative points were −10 km, 0 km, and 10 km in both X and Y directions to cover the survey area . In the Z direction, representative points were selected at cell indices k = 11, 21, 31, and 41, where k denotes the cell index in the depth direction. Here, k = 11 corresponds to the topmost cell just below the air layer, i.e., the first cell beneath the surface. Because topography is included, the physical depth associated with a given k varies with (X,Y); accordingly, we refer to vertical levels by the index k — constant-elevation slices relative to the model datum—rather than by a single fixed

depth below the local surface (Figure 3). We chose the k as we can cover the depth where we have interest.

In such ensemble analyses, the number of realizations generally needs to be comparable to the number of free parameters. Increasing the density to, for example, 5 × 5 × 4 or extending the point distribution would substantially enlarge the parameter space and require a far greater number of inversions. Given that each 3-D MT inversion takes 15–24 hours (Table 1), such an expansion is impractical in typical geothermal exploration workflows.

We used ordinary Kriging with an isotropic linear variogram (slope = 4,000; nugget = 0) to interpolate values from the representative points to all model cells. The slope was chosen as a pragmatic, grid-tied setting: a correlation length of approximately ten times the minimum horizontal cell size yielded spatially coherent initial models without oversmoothing. We did not attempt systematic optimization, prioritizing practical settings. Because 3-D MT inversion with smoothness regularization rapidly damps fine-scale structures in the starting model, the influence of detailed variogram tuning on the final results is expected to be limited. Our primary objective is to control the broad spatial patterns of the initial model rather than to optimize small-scale variability; therefore, we adopted this pragmatic variogram setting without further optimization.

Inversions for each initial model were performed on four independent computers. Since each inversion is independent, the workflow is trivially parallelizable across multiple computing nodes. The specifications of these machines are listed in Table 1. A typical inversion required 15–24 hours on a workstation equipped with an Intel i7–i9 CPU and 64 GB RAM. Runs 4 and 5 were executed on a 128 GB machine,

but two inversions were performed simultaneously; therefore, 64 GB RAM is sufficient for a single run. We also summarized the inversion settings in Table 2.

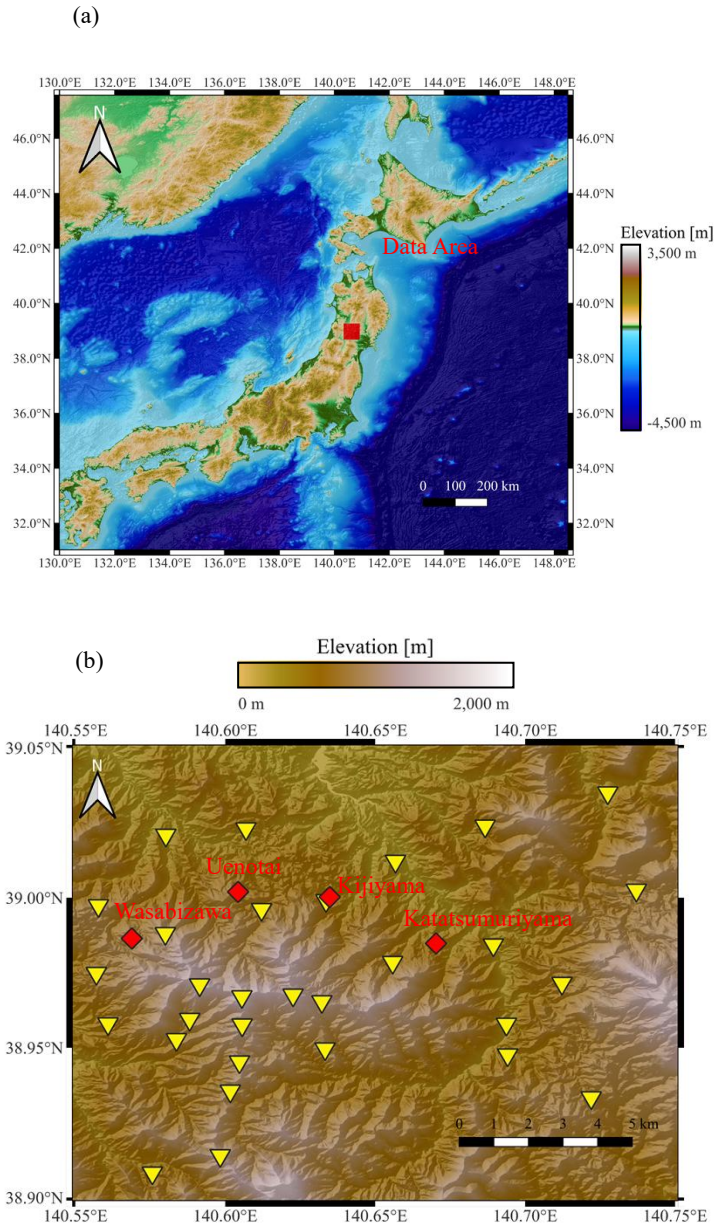

Figure 2

Maps showing (a) the broader region around Japan and (b) the study area.

Yellow triangles indicate MT observation sites, and red diamonds denote geothermal power plants either under construction or in operation. These maps were created using the GSI Fundamental Geospatial Data (Digital Elevation Model, 10 m mesh) (Geospatial Information Authority of Japan (GSI), 2025).

(a)

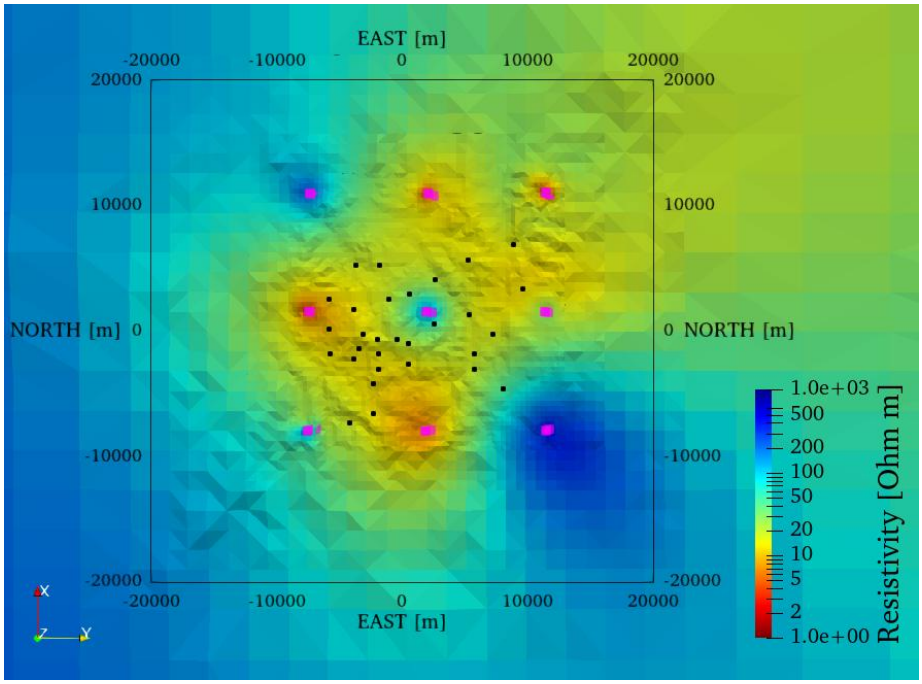

(b)

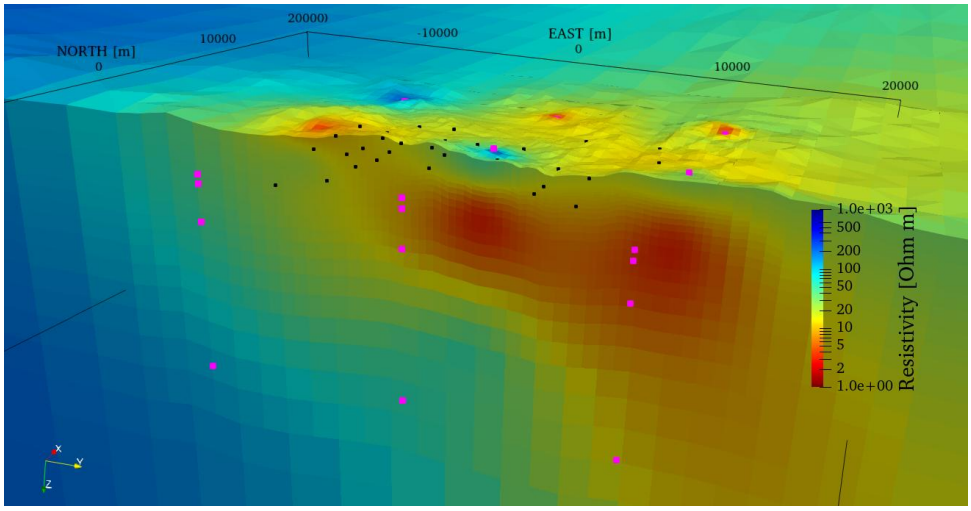

Figure 1

(a) **Plan view and (b) oblique view of a sample generated initial model.**

Colors indicate resistivity, and blue lines outline the mesh cells. Black points in (a) indicate the observation sites. Pink points in (b) represent the representative points.

Table 1

Specifications of the computers and the required inversion times. The preprocessing time for preparing the input files (a few minutes per case) is not included in the total inversion time.

	CPU	Memory	Cases	Total Inversion Time (h)	Avg. Time / Case (h)	Notes
Run 1	Intel Core i7-9700	64GB	17	394.3	23.2	
Run 2	Intel Core i9-10900	64GB	20	381.7	19.1	
Run 3	Intel Core i7-14700	64GB	25	388.3	15.5	
Run 4	Intel Core i9-14900K	128GB	18	359.3	20.0	Run 4 and Run 5 were performed simultaneously in the same computer.
Run 5	Intel Core i9-14900K	128GB	20	362.7	18.1	

Table 2

Summarization of inversion parameters

Category	Parameter	Value / Description
Data	MT responses	4 impedance tensor components + 2 tipper components
	Number of sites	30
	Frequencies	12 frequencies, 100 Hz – 0.001 Hz
	Error floors	5% for impedance tensor, 15% for tipper
Model domain & mesh	Domain size	200 km × 200 km × 160 km
	Grid size	34 × 34 × 62 cells (including 10 air layers)
	Total cells	210,297
	Min. cell size	400 m (X), 400 m (Y), 30 m (Z)
	Mesh refinement	Locally refined around survey area
	Topography	Included using ETOPO 2022 with unstructured hexahedral cells
	Air/sea resistivity	Constant values (air: 10^6 , sea: 0.25 Ω·m)
Initial model	Parameterization	3 × 3 × 4 representative points (36 parameters)
	Sampling range	$\log_{10}\rho \in [0, 3]$ (1–1000 Ω·m)
	Interpolation	Ordinary Kriging, isotropic linear variogram (slope = 4000, nugget = 0)
Inversion settings	Objective function	Data misfit + model smoothness + distortion tensor estimation
	Regularization parameters	$\lambda\_m = \lambda\_d$; sequence 10 → 1 → 0.1
	Final models evaluated at	$\lambda = 0.1$
	Distortion tensor	Estimated simultaneously
	Solver	3-D MT inversion code of Suzuki (2025)
Computation	Number of realizations	100 initial models
	Selected models	55 realizations with final RMS ≤ 2.15
	Inversion time	15–24 hours per realization (Table 1)
	Parallelization	Realizations run independently on 4 workstations

Results and Discussion

1. Realization set and selection criteria

To evaluate which realizations should be regarded as well-converged, we examined how the subsurface structure varies with respect to the final RMS values. Figure 4 shows that the distribution of the final RMS appears bimodal under the present sampling, suggesting the presence of two groups of solutions obtained from different initial models. To determine an appropriate RMS threshold separating these clusters, we analyzed the depth-averaged resistivity structure obtained from realizations selected under different RMS cutoffs. For each cutoff value, only realizations with RMS lower than that threshold were retained, and the depth-averaged resistivity in each depth interval D_k was computed as

$$\rho(D_k) = \frac{1}{\mid D_k \mid} \sum_{i \in D_k} \rho_i \,, \tag{5}$$

where ρ_i is the resistivity of cell i, $\mid D_k \mid$ is the number of cells belonging to the bin, and $\rho(D_k)$ represents the averaged resistivity within that depth layer. To keep the depth intervals approximately aligned with the original mesh layering, we used a constant bin thickness of 30 m for the upper three bins and increased the thickness geometrically with a multiplier of 1.15 for deeper bins. The resulting depth-averaged resistivity profiles (Figure. 5) show that realizations with lower RMS values (RMS ≤ 2.0, 2.15, 2.30, and 2.50) form a stable and nearly identical family of solutions: their depth-averaged structures overlap almost entirely and exhibit no systematic deviations. In contrast, realizations with higher RMS (RMS ≤ 2.7, 3.0) values exhibit clearly different depth-averaged profiles and form a separate group, consistent with the second mode of

the RMS histogram. This correspondence between the bimodal RMS distribution and the grouping of depth-averaged profiles indicates that the two RMS modes represent distinct solution clusters. Therefore, realizations belonging to the lower-RMS mode are interpreted as well-converged solutions, while those associated with the higher-RMS mode correspond to a different local minimum.

Next, to evaluate whether the 55 initial models adequately sample the model space, we assessed the stability of the ensemble statistics using a nonparametric bootstrap approach. Specifically, 100 bootstrap resamples were generated by randomly drawing 55 models with replacement from the original ensemble. For each resample, we computed a *depth-averaged standard-deviation curve* as follows. First, the vertical domain was divided into depth bins $\{D_k\}$. For each cell $i$falling within bin D_k, we calculated the standard deviation of the bootstrap values,

$$s_i = \sqrt{\frac{1}{N-1}\sum_{j=1}^{N}(m_{j,i} - \bar{m}_i)^2}, \tag{6}$$

where $m_{j,i}$ is the value of cell i in bootstrap realization j, and $\bar{m}_i$ is its ensemble mean. The depth-averaged standard deviation associated with bin D_k was then defined as

$$S(D_k) = \frac{1}{\mid D_k \mid}\sum_{i \in D_k} s_i\,, \tag{7}$$

where $\mid D_k \mid$ denotes the number of cells in the bin. The choice of the depth is the same as Figure 5. The resulting function $S(D_k)$ provides a depth-dependent measure of ensemble variability, which we refer to as the *depth-averaged standard-deviation curve*. Figure 6(a) shows the curves obtained for all bootstrap realizations.

Additionally, we computed the 95% bootstrap confidence interval (CI) from the 100 bootstrap realizations.

At each depth bin D_k, the lower and upper bounds of the CI were defined as the 2.5th and 97.5th percentiles of the bootstrap estimates, denoted as $S_{\mathrm{lower}}(D_k)$ and $S_{\mathrm{upper}}(D_k)$, respectively.

The CI width is therefore

$$W(D_k) = S_{\mathrm{upper}}(D_k) - S_{\mathrm{lower}}(D_k). \tag{8}$$

To obtain a dimensionless measure of sampling uncertainty, we computed the *relative confidence-interval width* by normalizing the CI width by the original spread estimate:

$$R(D_k) = \frac{W(D_k)}{S_{\mathrm{orig}}(D_k)}, \tag{9}$$

where $S_{\mathrm{orig}}(D_k)$ is the depth-averaged standard deviation computed from the full set of 55 realizations (Figure 6(b)). The profile $R(D_k)$provides a depth-dependent indicator of how strongly the estimated ensemble spread may fluctuate due to the finite size of the initial-model ensemble.

Figure 6(a) shows that all bootstrap realizations reproduce nearly identical depth-averaged standard-deviation curves. This consistency indicates that the ensemble of 55 initial models provides a sufficiently stable sampling of the model space, because the depth-dependent behaviour of the spread does not change appreciably under bootstrap resampling.

Furthermore, as shown in Figure 6(b), the width of the 95% confidence interval does not systematically increase with depth, suggesting that the sampling uncertainty of

the spread estimate remains relatively uniform throughout the model domain. Therefore, although the relative confidence-interval width is on the order of ~30%, the present ensemble size is adequate for reliably capturing the overall pattern and magnitude of model variability. Accordingly, in the following sections we treat the set of 55 realizations as a statistically representative sample of the underlying model population and base our interpretation on this ensemble.

Figure 7 illustrates the relationship between the initial and final RMS values of the realizations. Realizations with initial RMS values exceeding approximately 10.5 consistently failed to converge. For realizations with initial RMS values below this threshold, however, little correlation is observed between the initial and final RMS. This highlights the importance of exploring a diverse set of initial models.

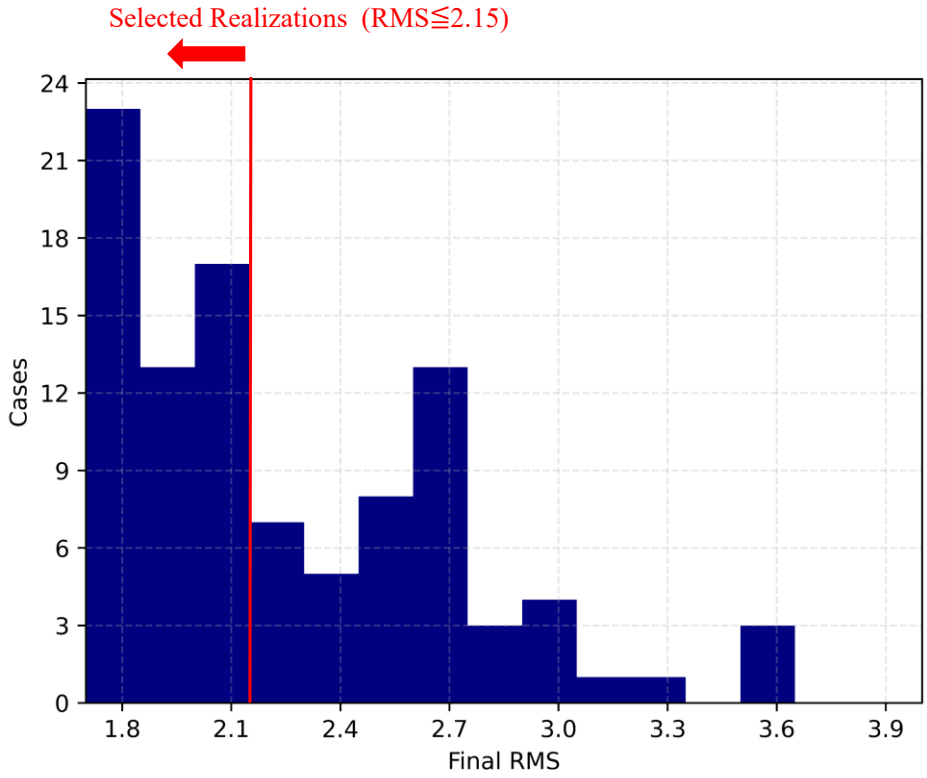

Figure 2

Histogram of final RMS values

Realizations with RMS values below 2.15 were selected for further analysis based on this distribution.

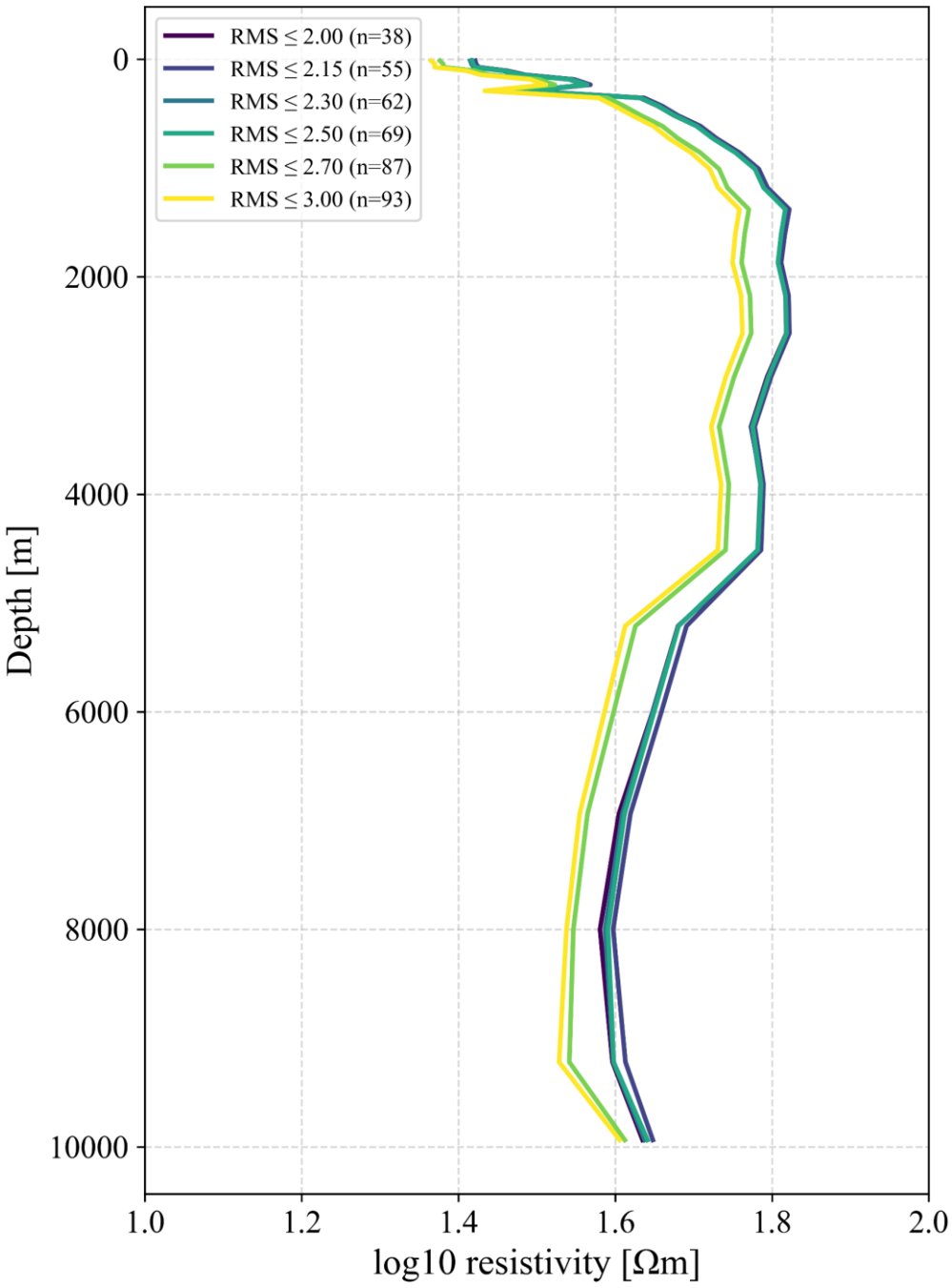

Figure 5

Depth-averaged resistivity profiles for ensembles selected with different RMS thresholds.

The value *n* in the legend denotes the number of realizations satisfying each RMS criterion.

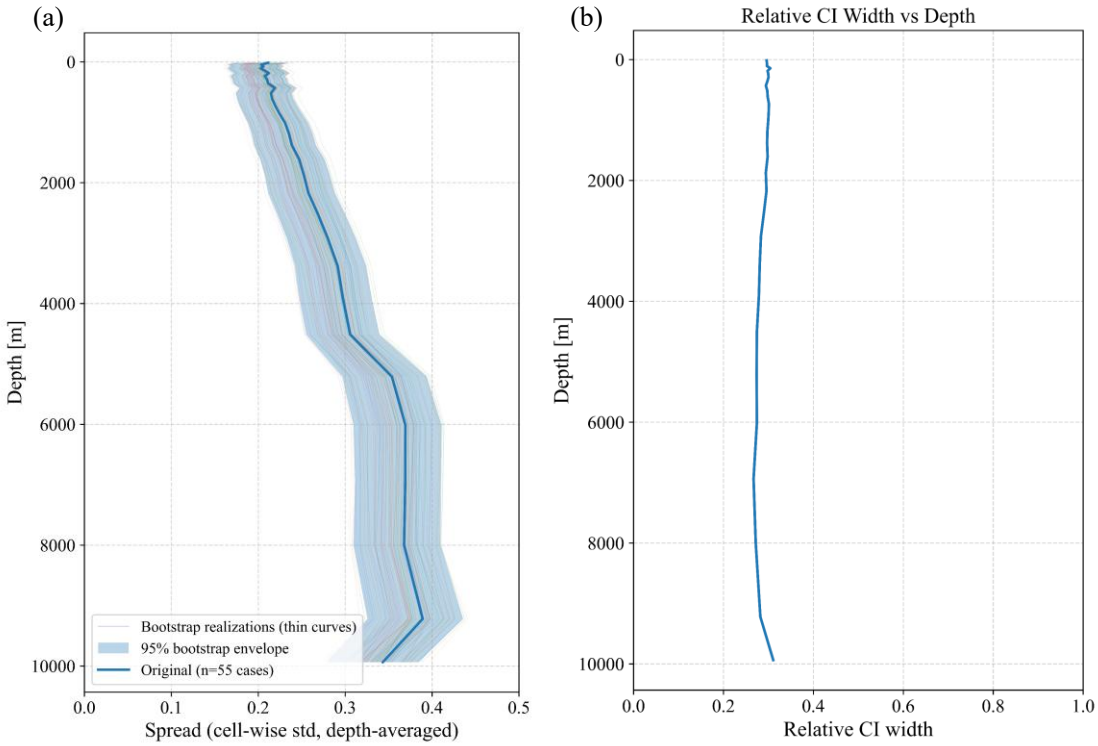

Figure 6

Bootstrap analysis of ensemble spread.

(a) Depth-averaged standard-deviation curves obtained from 100 bootstrap resamples; the shaded band shows the 95% bootstrap confidence interval, and the thick line denotes the original estimate (n = 55).

(b) Relative width of the 95% bootstrap confidence interval as a function of depth.

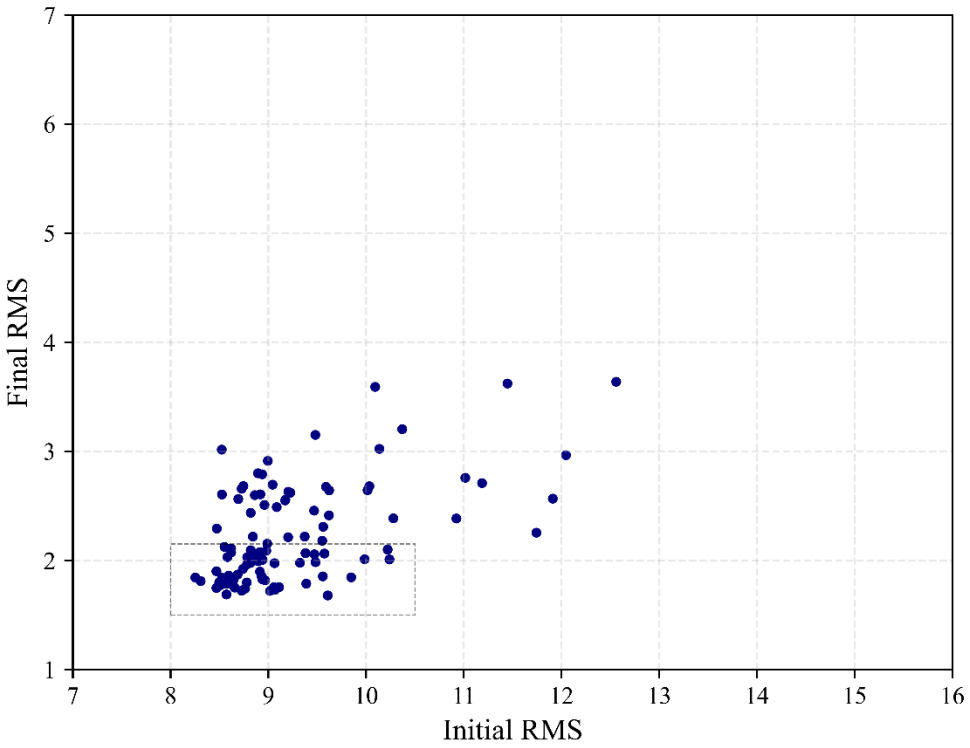

Figure 7

Scatter plot of initial versus final RMS values

The black dashed square indicates the selection region, where final RMS values are less than or equal to 2.15.

2. Geothermal Implications from the Resistivity and Uncertainty Structure

Figure 8 and 9 show the inversion results of mean resistivity and standard deviation structures. Figure 8(a) presents a vertical section at north = 500 m, and Figure 8(b) shows a corresponding section at east = 500 m. We interpret conductive region C1 as the cap layer as Ishizu et al. (2022). Laboratory and compilation studies indicate that clay-rich materials can exhibit a wide range of bulk resistivities, typically from about 1 to several tens of Ωm (Mutebi et al., 2020), depending on clay content, pore-fluid chemistry, and saturation conditions. In our model, the shallow conductor interpreted as the cap layer generally shows resistivities of several tens of Ωm, which falls within the broad resistivity spectrum expected for clay-rich cap rocks, although the shallow conductor is imaged in a relatively smoothed form and its fine-scale internal structure remains unresolved. In some areas, however, the ensemble standard deviation reaches approximately 0.3 log10 units (S in Figure 8), corresponding to an uncertainty of roughly a factor of two. In such regions, the absolute resistivity can vary substantially, and the contrast between conductive and more resistive altered units may not be sufficiently clear to ensure a robust cap-rock interpretation. These zones of larger uncertainty therefore highlight locations where interpretation should be made with particular caution, and where the uncertainty analysis can provide valuable information for assessing whether additional investigation or complementary surveys may be warranted. Such information is highly relevant for geothermal exploration because uncertainty in the position of the low-resistivity cap rock directly affects interpretations of reservoir depth and thickness, as well as the perceived continuity of cap-rock structures. Quantifying this uncertainty therefore provides information that can

contribute to more cautious and uncertainty-aware interpretation in geothermal exploration.

Figure 9 shows resistivity and standard deviation slices at depth. The conductive anomaly C2 broadly corresponds to the deep conductive zone reported by Ishizu et al. (2022), which Nunohara (2023)noted to be situated within the horst structure bounded by faults L1, L2, and L3. In our ensemble results, C2 also tends to follow this overall structural framework. The standard deviation distribution reveals a clear depth-dependent pattern: variability is generally small around 1 km depth but increases markedly with depth, especially on the outer side of C2 near L2 and L3. This indicates that the boundary of C2 is relatively well constrained on the L1 side, whereas the L2–L3 side exhibits substantially larger uncertainty at greater depths. Such spatial variability in uncertainty provides valuable information for geothermal development in deep high-temperature regions, helping to identify areas where structural interpretations are relatively robust and areas where additional investigations or more cautious assessment may be required.

Ishizu et al. (2022) interpreted the deeper portion of C2 below the silica sealing horizon as a zone potentially associated with supercritical conditions. Given this context, the depth-dependent uncertainty structure identified in our ensemble results provides useful information when evaluating deep high-temperature resources, including potential supercritical targets. Our analysis shows that the reliability of the inferred reservoir boundary varies substantially with both depth and location. In particular, the pronounced variability of the C2 boundary on the L2–L3 side indicates that drilling in this area may involve higher geological risk, thereby offering direct support for risk-aware well siting. In contrast, regions with smaller uncertainty, such as the vicinity of L1, provide more reliable structural constraints and can be regarded as

lower-priority areas for additional geophysical investigation. In this way, distinguishing between well-constrained and poorly constrained regions based on the uncertainty distribution provides useful guidance for the further utilization of the subsurface structural model.

It should be noted that the uncertainty patterns described here are derived solely from the publicly available MT dataset and from the inversion framework adopted in this study. In practical geothermal development, these MT-based constraints are typically supplemented by geological, geochemical, drilling, and monitoring data. The present results should therefore be regarded as one component of a broader, multi-disciplinary interpretation workflow to which our approach can contribute.

The uncertainty analysis presented in this study can therefore contribute to geothermal development planning in deep high-temperature environments by supporting interpretation reliability assessments, identifying the need for supplementary surveys, and reducing geological risk in decision-making.

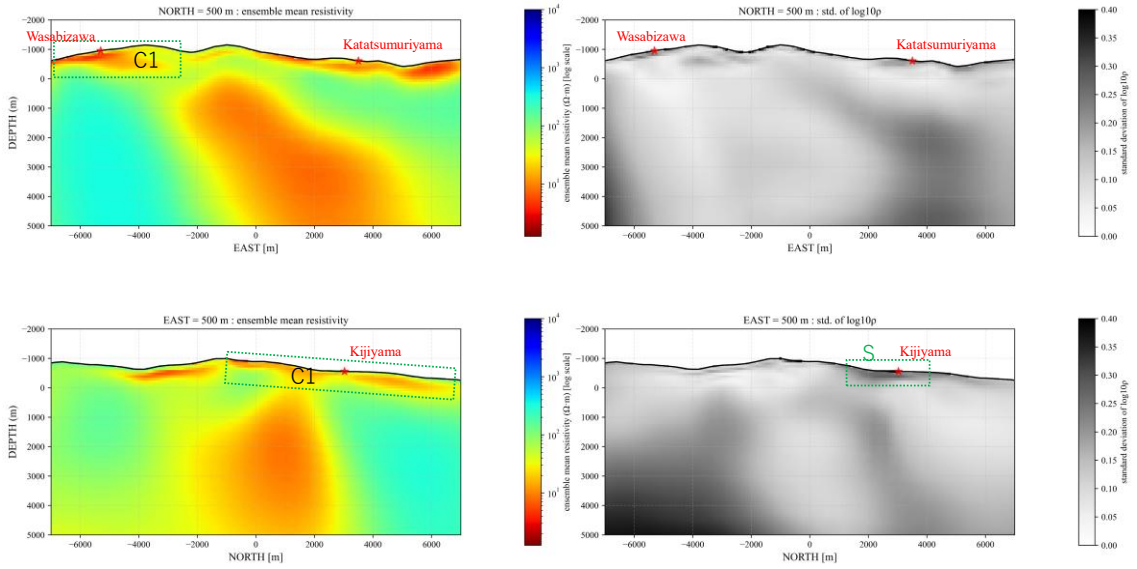

Figure 8

Vertical cross-sections of ensemble mean resistivity and standard deviation.

(a) Ensemble mean resistivity (left) and standard deviation of $\log_{10}\rho$ (right) along the NORTH = 500 m section.

(b) Same quantities shown for the EAST = 500 m section.

The shallow conductive feature C1 and the region of larger variability S are marked in the panels. Red stars mark geothermal power plants. Surface topography is displayed as the black curve.

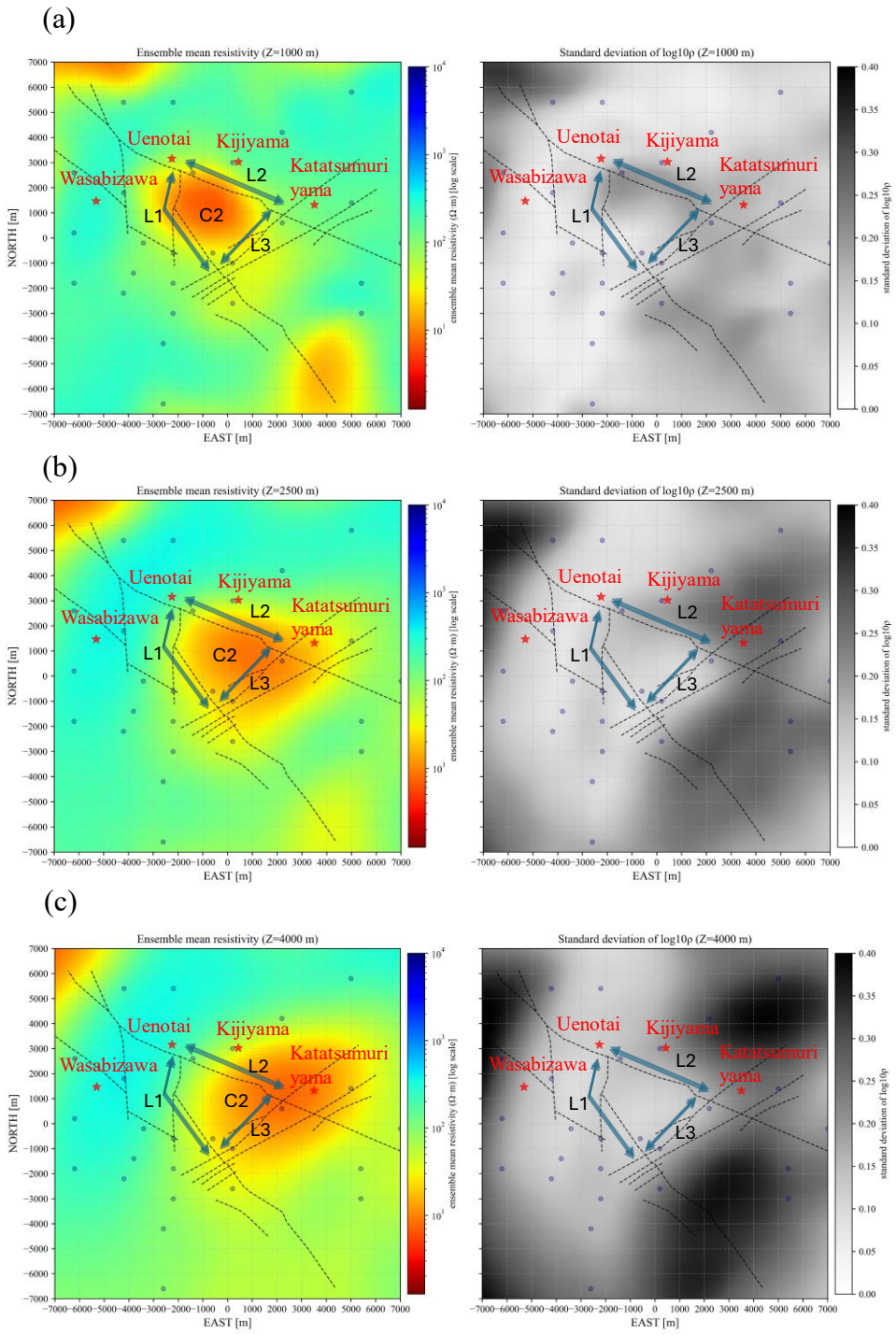

Figure 9

Horizontal slices of ensemble mean resistivity and standard deviation at selected depths.

(a) Ensemble mean resistivity (left) and standard deviation of $\log_{10}\rho$ (right) at Z = 1000 m, (b) Same quantities at Z = 2500 m, and (c) Same quantities at Z = 4000 m.

Fault traces (L1–L3) and the conductive anomaly C2 are indicated. Blue circles denote MT stations, and red stars mark geothermal power plants.

3. Scope and limitations

Although uncertainty in MT inversion arises from several ingredients—including error floors, regularization strength, and the structural parameterization—their effects tend to accumulate rather than cancel each other. In practice, if a region of the model is sensitive to even one influential factor (such as the initial model), that region is generally weakly constrained in the broader inversion problem. Therefore, areas showing large variability in our initial-model ensemble are expected to remain weakly constrained even if other inversion parameters were modified.

The initial model parameterization uses $3 \times 3 \times 4$ representative points on a regular lattice; we did not optimize their locations. Consequently, strong spatial anisotropy or layering not aligned with the lattice could bias the ensemble. A systematic study of point placement and density, in relation to the variogram ranges, is left for future work.

The computational requirements are also a key consideration for practical uncertainty analysis. Table 1 summarizes the inversion time on each computing system. In our environment, the total runtime was approximately 20 days, including interruptions due to system updates. This is considered practical, since magnetotelluric field data are typically acquired over periods of several months to years. We acknowledge, however, that the total runtime may become significant for larger surveys, finer meshes, or substantially increased ensemble sizes. Because each realization is fully independent, the workflow scales efficiently with parallel computing resources, but very large 3-D MT problems may still require cluster-level hardware or reduced-order formulations. This represents a practical limitation of ensemble-based uncertainty analysis.

Although the current number of realizations is insufficient for a comprehensive statistical characterization of the parameter space, it is adequate for examining typical variability and identifying robust trends. Furthermore, the workflow is embarrassingly parallel, allowing the number of realizations—and thus the robustness of the statistical results—to be readily increased with additional computing resources.

Conclusion

This study presents a practical and computationally efficient framework for evaluating uncertainty in three-dimensional magnetotelluric (MT) inversion results arising specifically from differences in the initial model. By parameterizing the starting resistivity distribution using a limited number of representative points and generating smooth initial models through Kriging interpolation, the proposed approach enables systematic exploration of plausible initial conditions while remaining computationally feasible for large-scale 3-D MT problems.

Application to the Yuzawa MT dataset demonstrates that, within the constraints of the present data and inversion framework, the ensemble-average resistivity structure consistently reproduces a shallow conductive zone. While the overall geometry of this shallow conductor is robust across realizations, the associated standard-deviation maps reveal localized regions of elevated uncertainty, reaching approximately 0.3 $\log_{10}$ units. These results indicate that resistivity contrasts and detailed boundaries may be less well constrained than suggested by a single best-fitting model.

At greater depths, a deeper conductive body broadly follows the structural framework delineated by major fault systems, but its lateral extent exhibits substantially larger variability among realizations. In particular, one side of the conductor remains relatively stable across the ensemble, whereas the opposite side shows increasing

variability with depth. This depth-dependent increase in variability suggests that interpretations of deeper conductive structures are more sensitive to initial-model choice than those of shallow features. Regions characterized by low ensemble variability can therefore be regarded as more robustly constrained, whereas areas of high variability indicate weaker constraints imposed by the MT data under the present inversion settings.

To assess whether the ensemble sufficiently samples initial-model-induced variability, we examined both the distribution of final RMS misfits and the statistical stability of the ensemble. The RMS distribution appears bimodal under the present sampling, and realizations with RMS values below a selected threshold form a consistent family in terms of depth-averaged resistivity profiles. Bootstrap resampling further indicates that the depth-dependent variability estimates are statistically stable, suggesting that the accepted ensemble provides an adequate basis for characterizing typical variability associated with differences in the initial model.

Although the proposed framework does not account for all possible sources of inversion uncertainty—such as data noise, regularization choices, or alternative structural parameterizations—it provides a transparent and operationally realistic lower-bound estimate of model variability under fixed inversion conditions. Because the workflow is embarrassingly parallel and does not require modification of the inversion algorithm, it can be readily integrated into existing MT inversion practices. By explicitly identifying which parts of an MT-derived resistivity model are robust and which are weakly constrained due to initial-model dependence, the proposed approach supports uncertainty-aware interpretation of MT inversion results in applied geophysical studies.

Data Availability

The inversion codes used in this study are openly available at GitHub: https://github.com/SuzukiAtsushi19911107/FV3DMT.

The MT dataset analyzed here was originally collected by Ishizu et al. (2022) in the Yuzawa geothermal field. The dataset can be downloaded from https://ds.iris.edu/spud/emtf.

The other data supporting the findings of this study is available from the corresponding author, upon reasonable request.

A preprint version of this manuscript has also been deposited on EarthArXiv (DOI: https://doi.org/10.31223/X5NM9X).

Declaration of Competing Interest

The authors declare no known competing financial interests or personal relationships that could have appeared to influence the work reported in this paper.

Funding

This research did not receive any specific grant from funding agencies in the public, commercial, or not-for-profit sectors.

Use of Generative AI

During the preparation of this work the author used ChatGPT in order to revise the grammar, style, and concision. After using this tool/service, the author reviewed and edited the content as needed and takes full responsibility for the content of the publication.

Acknowledgements

We thank colleagues for helpful discussions and the team who acquired and published the Yuzawa MT dataset (Ishizu et al., 2022). We also acknowledge computing resources provided by our institution.

References

Causse, E. (2023). Ensemble scenario-based inversion: A new approach for estimating the uncertainty of resistivity models derived from 3D controlled source electromagnetic data. *Geophysical Prospecting*, *71*(5), 847–875. https://doi.org/10.1111/1365-2478.13351

Doherty, J. E., Fienen, M. N., & Hunt, R. J. (2011). *Approaches to Highly Parameterized Inversion: Pilot-Point Theory, Guidelines, and Research Directions Scientific Investigations Report 2010-5168*. https://doi.org/10.3133/sir20105168

Ichiki, M., Kaida, T., Nakayama, T., Miura, S., Yamamoto, M., Morita, Y., & Uyeshima, M. (2021). Magma reservoir beneath Azumayama Volcano, NE Japan, as inferred from a three-dimensional electrical resistivity model explored by means of magnetotelluric method. *Earth, Planets and Space*, *73*(1). https://doi.org/10.1186/s40623-021-01451-y

Isaaks, E. H., & Srivastava, R. M. (1989). *An Introduction to Applied Geostatistics*. Oxford University Press.

Ishizu, K., Ogawa, Y., Nunohara, K., Tsuchiya, N., Ichiki, M., Hase, H., Kanda, W., Sakanaka, S., Honkura, Y., Hino, Y., Seki, K., Tseng, K. H., Yamaya, Y., & Mogi, T. (2022). Estimation of Spatial Distribution and Fluid Fraction of a Potential Supercritical Geothermal Reservoir by Magnetotelluric Data: A Case Study From Yuzawa Geothermal Field, NE Japan. *Journal of Geophysical Research: Solid Earth*, *127*(2). https://doi.org/10.1029/2021JB022911

Kelbert, A., Meqbel, N., Egbert, G. D., & Tandon, K. (2014). ModEM: A modular system for inversion of electromagnetic geophysical data. *Computers and Geosciences*, *66*, 40–53. https://doi.org/10.1016/j.cageo.2014.01.010

Li, J., Liu, J., Ogawa, Y., Guo, R., Wang, X., Wang, Y., Zhou, K., & Xu, J. (2025). Three-dimensional magnetotelluric inversion using an adaptive algebraic multi-resolution sampling approach. *Geophysics*, *90*(6), E225–E239. https://doi.org/10.1190/geo2024-0909.1

Macferrin, M., Amante, C., Carignan, K., Love, M., & Lim, E. (2025). The Earth Topography 2022 (ETOPO 2022) global DEM dataset. *Earth System Science Data*, *17*(5), 1835–1849. https://doi.org/10.5194/essd-17-1835-2025

Manassero, M. C., Afonso, J. C., Zyserman, F., Zlotnik, S., & Fomin, I. (2020). A reduced order approach for probabilistic inversions of 3-D magnetotelluric data I: general formulation. *Geophysical Journal International*, *223*(3), 1837–1863. https://doi.org/10.1093/gji/ggaa415

Muñoz, G., & Rath, V. (2006). Beyond smooth inversion: The use of nullspace projection for the exploration of non-uniqueness in MT. *Geophysical Journal International*, *164*(2), 301–311. https://doi.org/10.1111/j.1365-246X.2005.02825.x

Mutebi, D., Nur, A. A., Haryanto, A. D., & Wiwid, J. (2020). Variation of rock electrical resistivity in andesitic-trachytic volcanic geothermal areas. A case study of lili-sepporaki, Sulawesi Island-Indonesia. *Evergreen*, *7*(3), 314–322. https://doi.org/10.5109/4068609

NOAA National Centers for Environmental Information. (2022). *ETOPO 2022 15 Arc-Second Global Relief Model*. NOAA National Centers for Environmental Information. https://doi.org/10.25921/fd45-gt74

Nunohara, K. (2023). *Geothermal geology and resource assessment in the southern part of the Sanzu River Caldera, Northeastern Japan [in Japanese]*. Tohoku University.

Ogawa, Y., Honkura, Y., Ohtani, F., Kuroki, H., & Mitsuhata, Y. (1997). Preliminary Magnetotelluric Modeling in the Nikko Volcanic Area-Potential Break of Fluid Trap by Volcanic Intrusion. In *J. Geomag. Geoelectr* (Vol. 49).

Robertson, K., Thiel, S., & Meqbel, N. (2020). Quality over quantity: on workflow and model space exploration of 3D inversion of MT data. *Earth, Planets and Space*, *72*(1). https://doi.org/10.1186/s40623-019-1125-4

Sasaki, Y. (2004). Three-dimensional inversion of static-shifted magnetotelluric data. In *Earth Planets Space* (Vol. 56).

Siripunvaraporn, W., Egbert, G., Lenbury, Y., & Uyeshima, M. (2005). Three-dimensional magnetotelluric inversion: Data-space method. *Physics of the Earth and Planetary Interiors*, *150*(1-3 SPEC. ISS.), 3–14. https://doi.org/10.1016/j.pepi.2004.08.023

Suzuki, A. (2025). Development of a three-dimensional magnetotelluric inversion program considering topography with cell-centered finite volume method. *Earth Science Informatics*, *18*(1). https://doi.org/10.1007/s12145-024-01666-z

Usui, Y. (2015). 3-D inversion of magnetotelluric data using unstructured tetrahedral elements: Applicability to data affected by topography. *Geophysical Journal International*, *202*(2), 828–849. https://doi.org/10.1093/gji/ggv186

Zhang, T., Li, J., Ding, W., Kong, F., Fang, Y., Niu, X., Jiang, J., Yu, Z., Tan, P., Shen, Z., Yang, C., Sun, Q., Lu, Z., Yang, B., Liu, Y., Wang, Y., & Zhao, Y. (2025). Magnetotelluric evidence for highly focused mantle melting along the ultraslow-

spreading Gakkel Ridge, Arctic Ocean. *National Science Review*, *12*(5). https://doi.org/10.1093/nsr/nwaf077